Pergamon

Int. J. Heat Mass Transfer. Vol. 39, No. 17, pp. 3707–3716, 1996

0017-9310/96 $15.00 + 0.00

PII: S0017-9310(96)00003-8

Numerical computation of heat flow, fluid flow and interface shapes in the float zone of lithium niobate during a melting process

JYH-CHEN CHEN and HSIAN-KUN WU

Department of Mechanical Engineering, National Central University, Chung-Li, Taiwan 32054, Republic of China

(*Received* 8 *August* 1995 *and in final form* 8 *December* 1995)

Abstract—Computer simulations were performed to study the temperature and velocity distributions and the interface shapes in the floating-zone melt for lithium niobate materials. The input power distribution generated by the heat source was assumed to be Gaussian. The variation of the interface shapes and the transport phenomena in the flow zone relative to the input power was investigated. The results show that the shapes of the gas–melt and melt–solid interfaces and the temperature and velocity fields are modified by the gravity force; the influence of gravity increases as the input power increases. The present results are consistent with the recent experimental observations. Copyright © 1996 Elsevier Science Ltd.

1. INTRODUCTION

Refractory oxides absorb CO_2 lasers efficiently, since they have high absorption coefficients and low reflectivity near wavelengths of 10.6 μm [1]. Recently, CO_2 laser heating has been widely used in the float-zone crystal-growth process to produce single-crystal fibers of refractory oxides [2]. In this process, the material rod is heated uniformly by an axisymmetric ring-shape CO_2 laser beam with a high power density. A small molten zone with a steep temperature gradients at the growth interface is formed near the center of heating.

The heat and fluid transports and the interface shapes during the growth process influence the quality and structure of the resultant crystals. Since the melting point for most refractory oxides exceeds 1000 K, the melt is incandescent. Therefore, the transport phenomena and the interface shapes during the float-zone process are difficult to observe and measure. The measurement system may interfere with the transport phenomena during growth. Refractory oxides are semitransparent at the spectrum between the short-wavelength absorption edge (usually around ultraviolet) and the long-wavelength absorption edge (in the infrared), and they exhibit high absorption and low reflection at the spectrum between the long-wavelength absorption edge and the onset of the Reststrahlen bands. Chen and Hu [3, 4] employed a two-dimensional thermal radiometer to detect the thermal radiation from the heating area of a lithium niobate ($LiNbO_3$) rod during a CO_2 laser melting process. They used these radiative characteristics of refractory oxides to develop a method to observe the shapes of the solid–gas, solid–melt–gas, solid–melt, and melt–gas interfaces of the float zone and to find the temperature distribution during melting. Furthermore, they used these techniques to study the variation of the temperature distribution and interface shapes in the float zone relative to the input power [5]. The results of Chen and Hu [5] showed that the effect of the force of gravity increases with increasing input power. They suspect that for $LiNbO_3$ materials the interface shapes and the transport phenomena are strongly modified by gravity. At the current stage, the velocity field in the melt is still difficult to observe for materials with high melting points. To better understand the heat- and fluid-flow phenomena and the variation of the interface shapes during the floating-zone process, it is obvious that an appropriate numerical simulation, one that can take into account the relevant major physical phenomena, is needed. Of course, any such numerical model must be further verified by experiment.

Numerical simulations of the transport phenomena in the float-zone crystal-growth process have been performed by several authors [6–10]. Lan and Kou [6–8] assumed an ambient temperature distribution to study the velocity and temperature characteristics of $NaNO_3$ materials in the growth process. Chen and his co-workers [9–11] investigated the influence of the input power on both the thermocapillary flow and the shape of the float zone. Their results showed that the transport phenomena might be significantly different between fluids with lower and higher Prandtl numbers. For smaller Prandtl materials such as metals and semiconductors, the zone shape is determined primarily by the conductive heat transfer, while the influence of thermocapillary convection on the zone shape is not substantial. An increase in the input power is used mainly to increase the internal energy of the melt, and only a small portion of power is used

NOMENCLATURE

Bi_c	convection Biot number
Bi_r	radiation Biot number
Bo	static Bond number
Bo_{dyn}	dynamic Bond number
g	gravitational acceleration
Gr	Grashof number
h	surface heat transfer coefficient
H_l	convexity of the lower zone
H_u	convexity of the upper zone
$i_1(r)$	dimensionless shape function of the lower solid–melt interface
$i_2(r)$	dimensionless shape function of the upper solid–melt interface
k	thermal conductivity
Lc	inner zone length
Lc_l	inner zone length below $z = 0$
Lc_u	inner zone length above $z = 0$
Ls	outer zone length
Ls_l	outer zone length below $z = 0$
Ls_u	outer zone length above $z = 0$
p	pressure
P	dimensionless power
Pr	Prandtl number
q	power distribution
q_0	power density
Q	dimensionless power distribution
Q_0	dimensionless power density
r	dimensionless radial coordinate
r'	radial coordinate
$R(z)$	dimensionless position of the rod surface
$R'(z')$	position of the rod surface
Re	Reynolds number
Rt	T_∞/T_m
r_0	radius of the material rod
s	standard deviation of the Gaussian distribution
T	temperature
T_m	melting temperature
T_∞	ambient temperature
u	dimensionless radial velocity
V_l	dimensionless volume of the float zone
V_s	dimensionless volume of the float zone before it is melted
w	dimensionless axial velocity
z	dimensionless axial coordinate
z'	axial coordinate.

Greek symbols

α	thermal diffusivity
β	thermal expansion coefficient
γ	surface-tension temperature coefficient
Λ	thermal conductivity ratio
λ	density ratio
Θ	dimensionless temperature
Θ_{max}	maximum temperature
μ	dynamic viscosity
ν	kinematic viscosity
ε	emissivity
ρ	density
σ	Stefan–Boltzmann constant
σ_m	surface tension at the melting point
σ_t	surface tension gradient along the tangential direction of the gas–melt interface
ψ	stream function
Ψ	$\psi \cdot Pr \cdot Re$
θ_u	contact angle of the upper zone
θ_l	contact angle of the lower zone
ω	vorticity.

Subscripts

l	liquid phase
n	normal derivative on the solid–melt interface
s	solid phase.

to enlarge the float zone. Therefore, the strength of thermocapillary convection in the melt increases significantly with an increase in the input power. For higher Prandtl materials such as oxides, the input energy is transferred to the melt–solid interface by the stronger thermocapillary convection. As the input energy increases, only a small amount of power is converted into the internal energy of the melt, and an increase of the input power is mainly used to increase the size of the float zone. The temperature gradients in the melt do not increase significantly with an increase of the input power. They concluded that the thermocapillary instability of the melt in higher Prandtl materials may not appear before capillary instability (originating from the gas–melt interface) sets in. The influence of the deformable gas–melt interface is not included in their study.

In the present study, numerical computations were performed to investigate the variation of the transport phenomena in the melt and the interface shapes of the float zone with respect to the input power for $LiNbO_3$ materials during a CO_2 laser melting. The power distribution of the axisymmetric ring-shape laser beam impinging on the rod surface is assumed to be a Gaussian power distribution. The numerical scheme is a modified version of our previous investigations [9, 10] and includes the effect of the deformable gas–melt interface. The influence of gravity is also taken into account. The present results have been verified by recent experimental results [5].

2. THEORETICAL FORMULATION

Consider a circular rod of radius r_0 and of infinite length that is heated uniformly by a laser with an axisymmetric ring shape impinging on the center part of the rod. The laser power impinging on the surface of the rod of $LiNbO_3$ materials is attenuated completely and is assumed to be a Gaussian distribution,

$$q(z') = \frac{q_0}{s\sqrt{2\pi}} e^{-(1/2)(z'/s)^2}, \quad (1)$$

where the parameter q_0 is the density of the input laser power and s is the standard deviation of the distribution. About 99% of the input power lies in the region $-2.58s < z'/r_0 < 2.58s$. Chen and Hu [3] showed that the thermal radiation emitted from the heating rod of $LiNbO_3$ in the 3–5 μm spectrum is a volumetric phenomenon. Therefore, the influence of internal radiation on the heat transfer of the float zone may be significant. When the internal radiation is considered, the present problem becomes very complicated. To simplify the problem, the internal radiation of the heating rod is not taken into account. The input heat used to melt a small portion of the rod is dissipated by thermal convection and radiation from the rod surface. The system is at a steady state with no crystal growth. The float-zone model is shown in Fig. 1. The convection motion inside the melt, which is induced by variations in surface tension at the gas–melt interface and by the presence of the buoyancy force, is assumed to be axisymmetric and laminar.

The scales for length, velocity and pressure are taken to be r_0, $(\gamma T_m)/\mu$ and $(\gamma T_m)/r_0$, respectively, where μ is the dynamic viscosity of the melt, γ is the negative rate of change of surface tension with temperature, and T_m is the melting temperature. The dimensionless temperature is defined by $\Theta = (T - T_m)/T_m$. The dimensionless governing equations in the melt are of the following form:

$$Re\left(\frac{1}{r}\frac{\partial\psi}{\partial z}\frac{\partial\omega}{\partial r} - \frac{1}{r}\frac{\partial\psi}{\partial r}\frac{\partial\omega}{\partial z} - \frac{1}{r^2}\frac{\partial\psi}{\partial z}\omega\right) = \frac{\partial^2\omega}{\partial^2 r} + \frac{1}{r}\frac{\partial\omega}{\partial r} + \frac{\partial^2\omega}{\partial^2 z} - \frac{1}{r^2}\omega - \frac{Gr}{Re}\frac{\partial\Theta}{\partial r}, \quad (2a)$$

$$r\omega = \frac{\partial^2\psi}{\partial^2 r} - \frac{1}{r}\frac{\partial\psi}{\partial r} + \frac{\partial^2\psi}{\partial^2 z}, \quad (2b)$$

$$Pr \cdot Re\left(\frac{1}{r}\frac{\partial\psi}{\partial z}\frac{\partial\Theta}{\partial r} - \frac{1}{r}\frac{\partial\psi}{\partial r}\frac{\partial\Theta}{\partial z}\right) = \frac{\partial^2\Theta}{\partial^2 r} + \frac{1}{r}\frac{\partial\Theta}{\partial r} + \frac{\partial^2\Theta}{\partial^2 z}. \quad (2c)$$

In the solid region, the governing equation becomes

$$\frac{\partial^2\Theta}{\partial^2 r} + \frac{1}{r}\frac{\partial\Theta}{\partial r} + \frac{\partial^2\Theta}{\partial^2 z} = 0. \quad (2d)$$

Here, the stream function ψ and the vorticity ω are given by

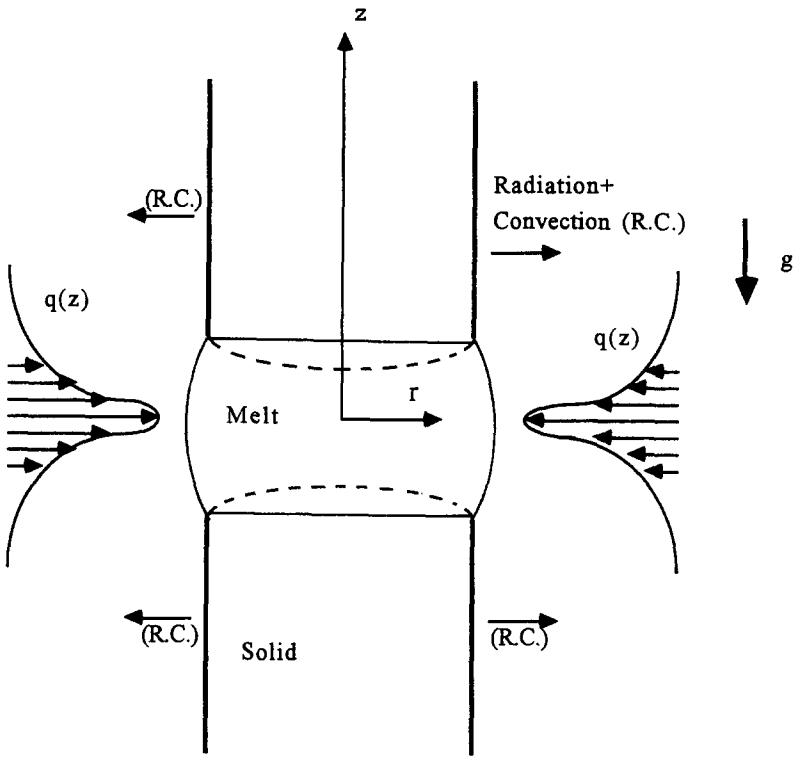

Fig. 1. Schematic diagram of the floating-zone system.

$$u = \frac{1}{r}\frac{\partial \psi}{\partial z}, \quad w = -\frac{1}{r}\frac{\partial \psi}{\partial r}, \quad \omega = \frac{\partial u}{\partial z} - \frac{\partial w}{\partial r}. \tag{3}$$

The three dimensionless parameters that appear in the equation (2) are

$$\text{Reynolds number:} \quad Re = \gamma T_m r_0/\mu\nu,$$

$$\text{Grashof number:} \quad Gr = \rho_l^2 g\beta T_m r_0^3/\mu^2,$$

$$\text{Prandtl number:} \quad Pr = \nu/\alpha,$$

where g is the gravitational acceleration, α is the thermal diffusivity, ν is the kinematic viscosity, β is the coefficient of volumetric expansion, ρ_s is the density of the solid region, and ρ_l is the density of the melt region.

There exist two unknown free boundaries in the present problem: melt–solid interface and melt–gas interface. At the melt–solid interface, the temperature is the melting point of the material, and the energy must be balanced. At the melt–gas interface, the velocity must satisfy the kinematic boundary condition, and the shear and normal stresses and energy must be balanced. The deformable shape of the melt–gas interface is governed by the normal-stress balance. The previous study [7] showed that the effect of convection on the melt–gas interface shape is very small and can be ignored. When the effect of convection on the normal-stress balance is not taken into consideration, the boundary condition is usually referred to as the Young–Laplace equation. To save computation time, the effect of convection is not taken into account in the present study when we locate the position of the melt–gas interface.

The appropriate thermal boundary conditions are as follows:

(i) symmetry at the center line,

$$\frac{\partial \Theta}{\partial r} = \psi = \omega = 0 \quad \text{at } r = 0; \tag{4a}$$

(ii) energy balance at the gas–solid interface,

$$-\frac{\partial \Theta}{\partial r} = Bi_r[(\Theta+1)^4 - Rt^4] + Bi_c(\Theta + 1 - Rt) - Q(z) \quad \text{at } r = 1; \tag{4b}$$

(iii) energy balance at the gas–melt interface,

$$-\Lambda\left(\frac{\partial \Theta}{\partial r} - \frac{dR}{dz}\frac{\partial \Theta}{\partial z}\right) = \left[1 + \left(\frac{dR}{dz}\right)^2\right]^{1/2}\{Bi_r[(\Theta+1)^4 - Rt^4] + Bi_c(\Theta + 1 - Rt) - Q(z)\} \quad \text{at } r = R(z); \tag{4c}$$

(iv) kinematic boundary condition on the deformable gas–melt interface,

$$\psi = 0, \quad \text{at } r = R(z); \tag{4d}$$

(v) shear stress balance at the deformable gas–melt interface,

$$\left[1 - \left(\frac{dR}{dz}\right)^2\right]\omega = \left[1 + \left(\frac{dR}{dz}\right)^2\right]^{1/2}\left(\frac{\partial \Theta}{\partial z} + \frac{dR}{dz}\frac{\partial \Theta}{\partial r}\right) + 2\frac{dR}{dz}\left(2\frac{\partial^2 \psi}{\partial r\,\partial z} - \frac{1}{r^2}\frac{\partial \psi}{\partial z}\right) + 2\frac{1}{r}\left[1 - \left(\frac{dR}{dz}\right)^2\right]\frac{\partial^2 \psi}{\partial z^2} \quad \text{at } r = R(z); \tag{4e}$$

(vi) normal stress balance at the deformable liquid–gas interface without including the convection effect,

$$p - Bo \cdot z + \frac{\dfrac{d^2R}{dz^2}}{\left[1 + \left(\dfrac{dR}{dz}\right)^2\right]^{3/2}} - \frac{1}{R\left[1 + \left(\dfrac{dR}{dz}\right)^2\right]^{1/2}} = 0 \quad \text{at } r = R(z); \tag{4f}$$

(vii) temperature equal to the melting point at the melt–solid interface,

$$\Theta = 0 \quad \text{at } z = i_1(r) \quad \text{and} \quad i_2(r); \tag{4g}$$

(viii) energy balance at the melt–solid interface,

$$\left(\frac{\partial \Theta}{\partial n}\right)_s - \Lambda\left(\frac{\partial \Theta}{\partial n}\right)_l = 0 \quad \text{at } z = i_1(r) \quad \text{and} \quad i_2(r); \tag{4h}$$

(ix) no slip and no penetration at the melt–solid interface,

$$\psi = 0, \tag{4i}$$

$$r\omega = \frac{\partial^2 \psi}{\partial^2 r} - \frac{1}{r}\frac{\partial \psi}{\partial r} + \frac{\partial^2 \psi}{\partial^2 z} \quad \text{at } z = i_1(r) \quad \text{and} \quad i_2(r); \tag{4j}$$

(x) no heat transfer far from the melt

$$\frac{\partial \Theta}{\partial z} = 0 \quad \text{as } z \to \pm\infty. \tag{4k}$$

The subscript n denotes the partial derivative in the normal direction on the solid–melt interface, while the subscripts s and l denote the solid and liquid phases, respectively. The function $Q(z)$ is given by,

$$Q(z) = \frac{Q_0}{s\sqrt{2\pi}} e^{-(1/2)(z/s)^2}. \tag{4l}$$

At the solid–melt–gas junction, we have

$$R(z = i_1(1)) = R(z = i_2(1)) = 1. \tag{4m}$$

In the present study, the material rod is melted without a crystal growth. Then the mass conservation

must be satisfied during the melting process. The principle of conservation of mass requires

$$\int_{V_l} \mathrm{d}v = V_l = \lambda V_s, \tag{4n}$$

where V_l is the dimensionless volume of the floating zone and V_s the dimensionless volume of the solid corresponding the float zone before it is melted. Kou and Lan [7, 8] considered the case that the crystal is growing steadily with a constant diameter. Therefore, they used a fixed contact angle at the gas–melt–solid trijunction, instead of the requirement of mass conservation in the melt.

The dimensionless parameters which appear in the boundary conditions (4) are:

dimensionless ambient temperature	$Rt = T_\infty/T_m$;
dimensionless power density	$Q_0 = q_0 r_0/(k_s T_m)$;
static Bond number	$Bo = \rho_l g r_0^2/\sigma_m$;
Biot number of radiation	$Bi_r = \varepsilon\sigma T_m^3 r_0/k_s$;
Biot number of convection	$Bi_c = h r_0/k_s$;
conductivity ratio	$\Lambda = k_l/k_s$;
density ratio	$\lambda = \rho_s/\rho_l$;

where T_∞ is the ambient temperature, ε is the emissivity, σ_m is the mean surface tension, σ is the Stefan–Boltzmann constant, q_0 is the power density, k_s is the thermal conductivity of the solid region, k_l is the thermal conductivity of the melt region and h is the surface heat transfer coefficient. The dimensionless power is defined by $P = 2\pi r_0 q_0/k_s T_m = 2\pi Q_0$.

3. SOLUTION PROCEDURE

The finite difference scheme employed previously by Chen *et al.* [9] and Chen and Chu [10] has been modified to solve system (2) with boundary conditions (4). The discrete form of the system is constructed using second-order central differencing. In the present problem, the shapes of the solid–melt and melt–gas interfaces are unknown beforehand and must be obtained as part of the solution. The computations are initiated by assigning an initial shape to the float zone. The physical domain is divided into three regions: one molten zone and two solid regions. A boundary-fitted curvilinear coordinate transformation was employed in the code to transfer the irregular physical domains to regular computational domains. Grid-stretching transformation were used to provide good resolution near the interfaces. Initial guesses for ψ, ω and T over the entire computation domain were chosen. The differential equations for the stream function, vorticity and temperature were solved iteratively using the line-successive over-relaxation (LSOR) method. The new shape of the melt–gas interface was determined from the requirements of normal stress balance equation (4f) and the conservation of mass equation (4n). The Stefan condition (4h) was used to check whether or not the melt–solid interface shape was correct.

Table 1. Physical properties of $LiNbO_3$ [12–14]

Properties	$LiNbO_3$
T_m [K]	1526
ρ_l [kg m^{-3}]	3.64×10^3
ρ_s [kg m^{-3}]	4.37×10^3
β [K^{-1}]	1.7×10^{-4}
ν [m^2 s^{-1}]	1.37×10^{-5}
α [m^2 s^{-1}]	2.5×10^{-7}
γ [N mK^{-1}]	4×10^{-4}
k_s [W mK^{-1}]	2.5
k_l [W mK^{-1}]	0.83
c_p [J (kg K)$^{-1}$]	919
ε	0.31
σ_m [N m^{-1}]	0.175

4. RESULTS AND DISCUSSION

The computational results for $LiNbO_3$ are based on the physical properties shown in Table 1. All computations are based on $Rt = 0.2$ and $Bi_c = 0$. The radius of the material rod considered was 0.75 mm. The corresponding dimensionless parameters in the earth environment are listed in Table 2. The dimensionless length of the rod was chosen to be 20. Grids were chosen as 41×31 in the crystal and feed-rod regions and 41×71 in the molten region. For convenience, the stream function was rescaled by $\Psi = \psi \cdot Pr \cdot Re$.

Figure 2 illustrates the influence of the force of gravity on the flow structure and the temperature field for $s = 0.3876$. There are two toroidal cells in the melt with the flow rising up near the heating center and sinking down near the solid–melt interface. Since the Prandtl number of the $LiNbO_3$ melt is about 55, the momentum diffusivity is much larger than the thermal diffusivity. Unlike the flow structure of Mo and Si materials (lower-Prandtl number fluids) [10], the four-cell flow structure has never been computed for the extent of the input power considered in the present study. The isothermals in the melt for $LiNbO_3$ materials are significantly modified by the thermocapillary flow. Larger temperature gradients in the axial direction appear near the melt–solid interface, while in the radial direction larger temperature gradi-

Table 2. Dimensionless parameters of $LiNbO_3$

r_0	0.75 mm
Pr	55
Re	134
Gr	5.58
Bi_r	0.0183
λ	1.2
Λ	0.33
Bo	0.118

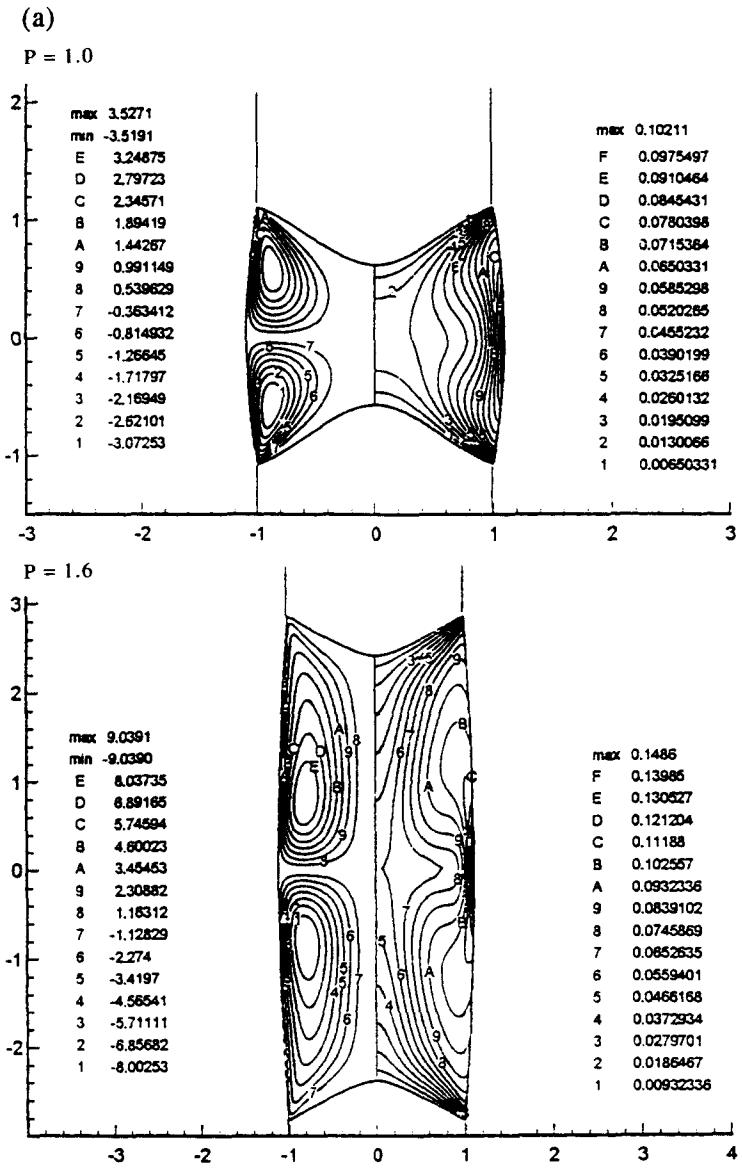

Fig. 2(a). Contours for streamlines and isothermals in the melt of $LiNbO_3$ for $s = 0.3876$ with two different P in a zero gravity environment.

ents occur near the heating center. In a zero gravity environment ($Gr = 0$ and $Bo = 0$), the velocity and temperature fields and the shape of the gas–melt interface are symmetric along the heating center. Also, the shape of the gas–melt interface is concave to the float zone for $P = 1.0$ and 1.6, since the volume of the float zone is larger than that of the solid before the melting, due to the fact that the density of the melt of $LiNbO_3$ is less than that of the solid. Therefore, the shape of the gas–melt interface is always concave to the melt in a zero gravity environment. In the earth environment, gravity has a strong influence on the shape of the gas–melt interface. For $P = 1.0$, the shape of the gas–melt interface is concave to the melt. When $P = 1.6$, the shape becomes convex to the melt at the upper zone and concave at the lower zone. The temperature and velocity fields in the melt are asymmetric due to the influence of gravity. In the present system, the buoyancy-driven motion enhances the strength of the thermocapillary flow in the upper zone, but it depresses the flow in the lower zone. Since the dynamic Bond number ($Bo_{dyn} = Gr/Re$), which usually characterizes the relative important of the buoyancy-driven convection and the thermocapillary convection, is very small, the influence of the buoyancy-driven convection is not significant. The shape of the gas–melt interface affects the size of the cross-sectional area in the axial direction. The amount of heat transfer in the axial direction is larger for a larger cross-sectional area. The force of gravity tends to decrease the size of the upper zone and increase that of the lower zone. The influence of gravity increases with increasing zone

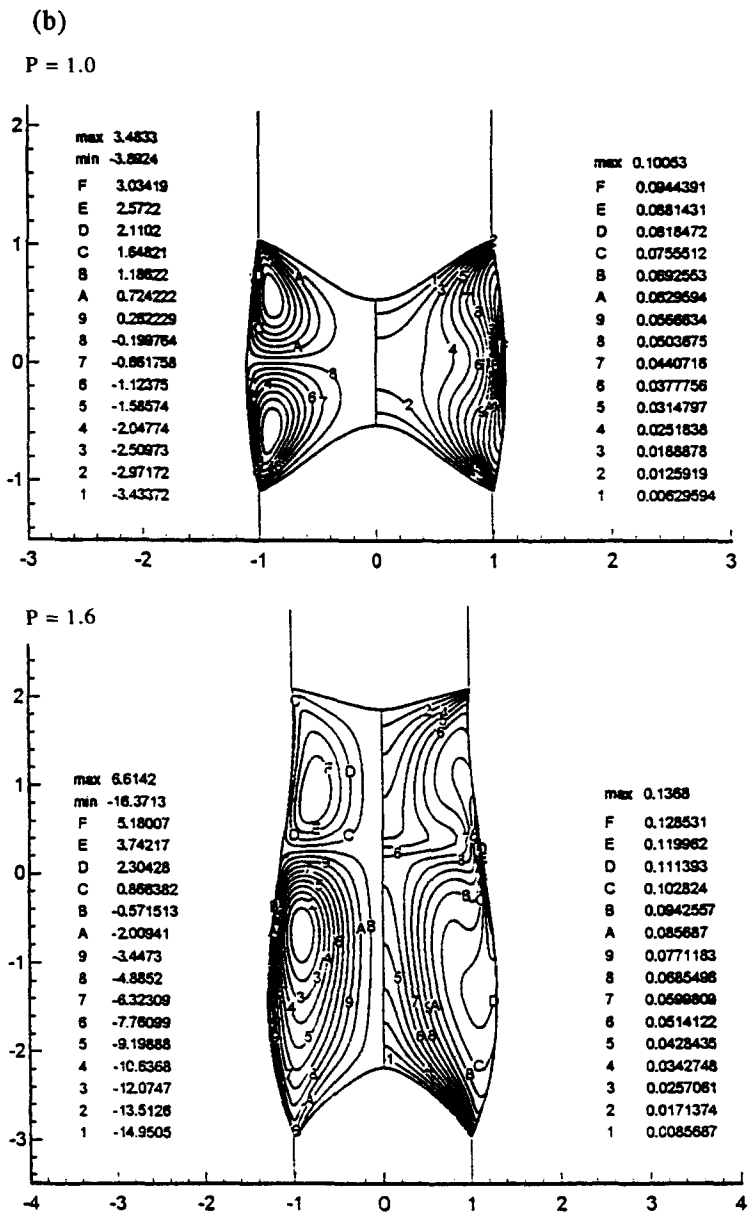

Fig. 2(b). Contours for streamlines and isothermals in the melt of $LiNbO_3$ for $s = 0.3876$ with two different P in the earth environment.

length. This is why, with an increase of the input power, the shape of the gas–melt interface changes from concave towards the melt to convex at the upper zone and concave at the lower zone. The experimental results of Chen and Hu [5] also show this trend. Therefore, the results in Fig. 2(b) show the strength and size of the lower cell to be larger than those of the upper cell, and the isothermals in the lower zone are more distorted than those in the upper zone. The difference increases with increasing input power.

Figure 3 shows the distribution of the gas–melt interface shape $R(z)$, surface tension gradient σ_t, and surface temperature of the float zone for $P = 1.4$ and $s = 0.7752$. From Fig. 3(a), it is clear that in a zero gravity environment the surface tension gradient is antisymmetric, and the shape of the gas–melt interface and the surface temperature is symmetric along the heating center ($z = 0$). The maximum temperature and the zero value of the surface tension gradient occur at the heating center. Since the input energy is carried to the melt–solid interface by the thermocapillary flow, the surface temperature decreases slowly away from the heating center and decreases rapidly near the melt–solid interface. The largest temperature gradient appears near the solid–melt interface. Figure 3(b) shows that in the earth environment the maximum temperature occurs below the heating center, and the zero value of the surface tension gradient appears above the heating center, which is the reflection point of the gas–melt interface shape and

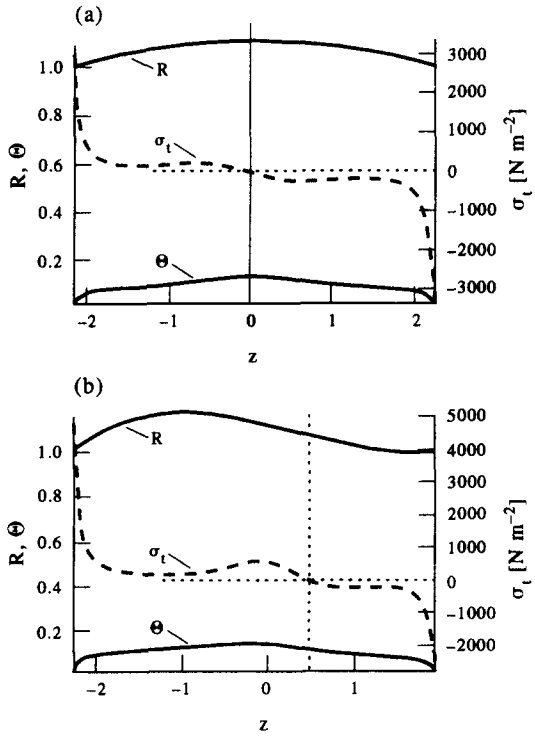

Fig. 3. Gas–melt interface, surface-tension gradient, and surface temperature of the float zone of $LiNbO_3$ for $P = 1.4$ and $s = 0.7752$: (a) zero gravity and (b) one gravity.

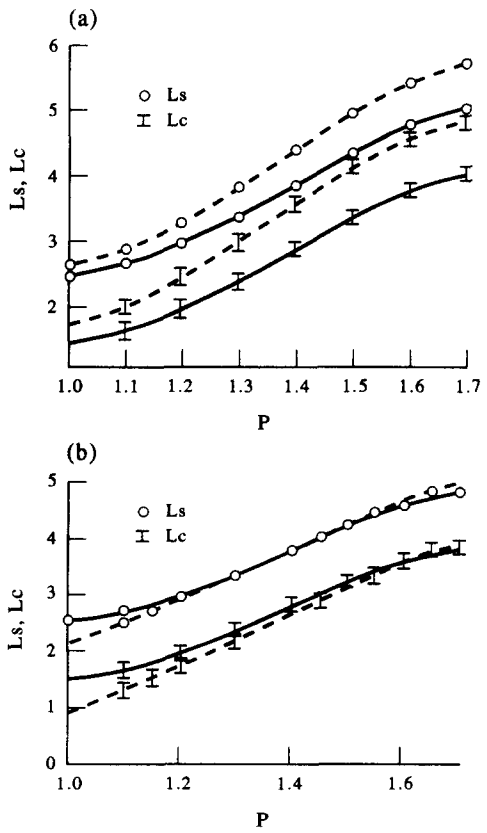

Fig. 4. (a) Zone lengths vs input power P for $LiNbO_3$ with and without the influence of gravity. The solid lines represent the results for the earth environment and the dashed line denotes the results for the zero gravity environment. (b) Zone lengths versus input power P for $LiNbO_3$ with different power distributions in the earth environment. The solid lines represent the results for $s = 0.3876$ and the dashed line denotes the results for $s = 0.7752$.

the location of the intersection of the upper and lower cells.

Figure 4 displays the effect of the input power on the zone length. In Fig. 4, Ls and Lc denote the outer and inner lengths of the float zone, respectively. The outer zone length is greater than the inner one, and the zone lengths increase as the input power increases. Therefore, the melt–solid interface is always convex to the melt in the present problem. Figure 4(a) shows that the zone length is decreased by gravity. The power distribution of $s = 0.3876$ is more condensed at the surface of the rod near $z = 0$ than it is for $s = 0.7752$. For a smaller input power, the zone lengths for $s = 0.3876$ are greater than those for $s = 0.7752$ [Fig. 4(b)]. The discrepancy decreases as the input power increases. In Fig. 5, Ls_u, Lc_u, Ls_l and Lc_l represent the outer and inner zone lengths above $z = 0$ and below $z = 0$, respectively. The results show that the increase rate of the lower zone length is faster than that of the upper zone with increasing input power. This trend is also observed in the experiments performed by Chen and Hu [5]. Figure 6 illustrates the effect of the input power and the power distribution on the maximum temperature Θ_{max} in the earth environment. The maximum temperature increases as the input power increases. For a specific input power, the maximum temperature for $s = 0.3876$ is higher than it is for $s = 0.7752$, because of the denser distribution near $z = 0$ for $s = 0.3876$. Figure 7 displays the maxima of the absolute value of the stream function in the upper and lower cells vs the input power for two different power distributions. The magnitude of the stream function increases as the input power increases. The strength of the stream function of the upper cell is smaller than that of the lower one. The difference increases significantly with increasing input power.

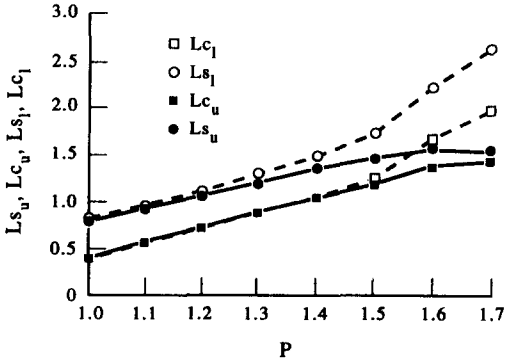

Fig. 5. Outer and inner lengths of the upper and lower zones vs input power P for $LiNbO_3$ with $s = 0.3876$ in the earth environment.

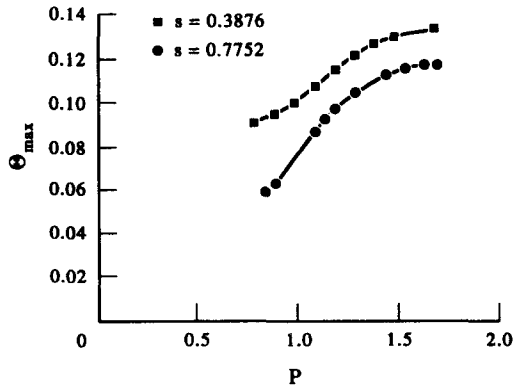

Fig. 6. Maximum temperature Θ_{max} vs input power P for $LiNbO_3$ with two different power distributions in the earth environment.

The convexity of the melt–solid interface is defined as

$$H_i = Ls_i - Lc_i,$$

where i = u or l. Figure 8 illustrates the variation of the convexity with the input power. Figure 8(a) shows the influence of gravity on the shape of the melt–solid interface. In a zero gravity environment, the convexity of the lower zone is the same as that of the upper zone, and the convexity decreases slightly and then increases slowly with a continuous increase of the input power. We can expect that the convexity is at a maximum when the molten zone is formed without a core. With further increases of the input power, the heat transfer in the axial direction becomes significant and the increase of the molten zone near the center is faster than it is in the region near the gas–melt interface, due to heat loss on the surface. Therefore, the convexity decreases as the input power increases. The axial heat transport due to thermocapillary convection is much more enhanced in the region near the gas–melt interface than it is near the center region. The strength of the thermocapillary convection increases with the

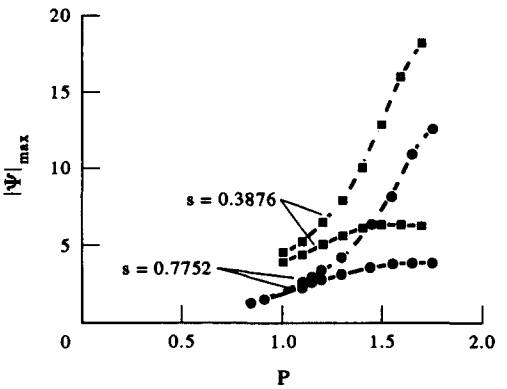

Fig. 7. Maxima of the absolute value of the stream function in the upper and lower cells vs the input power for two different power distributions. The solid lines represent the results for the upper cell and the dashed lines denote the results for the lower cell.

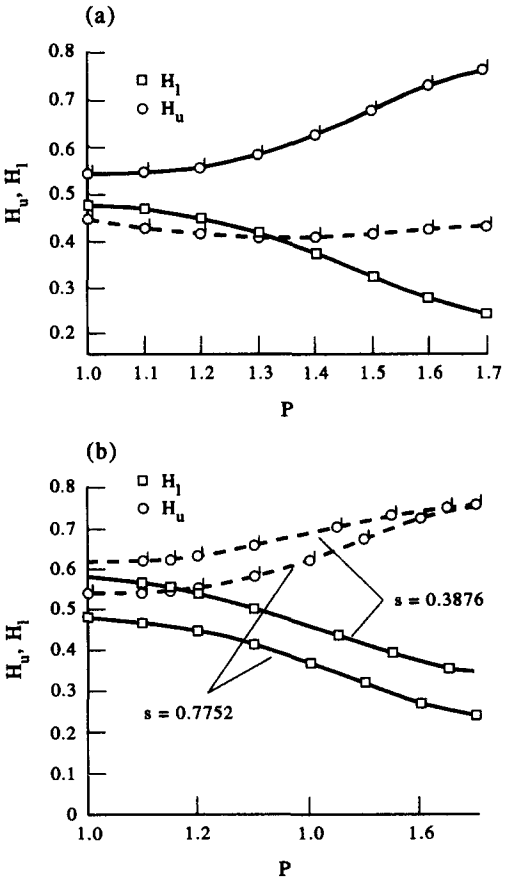

Fig. 8. (a) Convexities of the melt–solid interface for the upper and lower zones vs input power P for $LiNbO_3$ with $s = 0.3876$ in the zero-gravity and earth environments. The solid lines represent the results for the earth environment and the dashed line denotes the results for the zero gravity environment. (b) Convexities of the melt–solid interface for the upper and lower zones vs input power P for $LiNbO_3$ with two different power distributions in the earth environment.

input power. This is why the convexity increases with an increase of the input power after it reaches an extremum. In the earth environment, the thermocapillary convection in the upper region is depressed by the gravity force. Conversely, the thermocapillary convection in the lower region is enhanced by the gravity force. This is why in Fig. 8(a) the convexity of the upper zone decreases and that of the lower zone increases continuously as the input power increases. Since the strength of the thermocapillary flow for $s = 0.3876$ is stronger than that for $s = 0.7752$ for a given input power, the heat carried toward the melt–solid interface by the thermocapillary flow for $s = 0.3876$ is much larger than that for $s = 0.7752$. Therefore, the convexity for $s = 0.3876$ is larger than that for $s = 0.7752$.

The contact angle is defined as the angle between the tangent to the gas–melt interface at the gas–melt–solid trijunction and the axis of the rod. Figure 9 shows the variation of the contact angle with the input power for $s = 0.3876$. In Fig. 9, we use θ_u and θ_l to

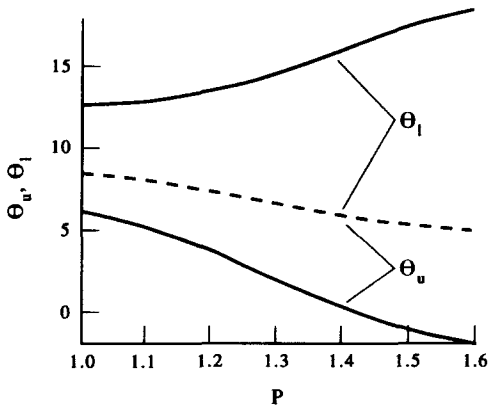

Fig. 9. Contact angle vs input power P for $LiNbO_3$ with $s = 0.3876$ in the zero-gravity and earth environments. The solid lines represent the results for the earth environment and the dashed line denotes the results for the zero gravity environment.

represent the contact angles of the upper and lower zones, respectively. Since in a zero gravity environment the gas–melt interface is always concave toward the melt and is symmetric along the heating center, the upper contact angle θ_u equals the lower contact angle θ_l, and they are always positive. The contact angle decreases as the input power increases. In the earth environment, the lower contact angle increases with increasing input power. As the input power increases, the upper contact angle changes from positive to negative. These results are consistent with those observed by Chen and Hu [5].

5. CONCLUSIONS

Computations were performed to investigate the temperature and velocity fields and the interface shape in the float-zone melting process for $LiNbO_3$. The shape of the gas–melt interface is significantly affected by the force of gravity. In a zero gravity environment, the shape of the gas–melt interface is always concave towards the melt. Due to the influence of gravity, the shape of the gas–melt interface changes from concave towards the melt to convex towards the melt at the upper zone, and concave towards the melt at the lower zone as the input power increases. This trend is consistent with that seen in the experiments [5]. The temperature and velocity fields and the shape of the melt–solid interface are modified significantly due to the change of the gas–melt interface shape. The influence of gravity on the velocity and temperature fields and on the zone shape increases significantly as the input power increases. For the input power considered in the present study, two toroidal cells always appear in the melt of $LiNbO_3$. The force of gravity enhances the strength of the thermocapillary flow of the lower cell, but it depresses the flow of the upper cell. The melt–solid interface is convex to the melt. Due to the effect of thermocapillary flow, the convexity of the lower zone increases and that of the upper zone decreases as the input power increases.

Acknowledgements—The authors gratefully acknowledge the National Science Council of the Republic of China for their support of this work through grant no. NSC83-0401-E008-004.

REFERENCES

1. G. A. Kobzev and V. A. Petrov, Behavior of thermal radiation properties of oxide ceramics under subsecond laser heating, *Int. J. Thermophys.* **14,** 371–381 (1993).
2. R. S. Feigelson, Pulling optical fibers, *J. Crystal Growth* **79,** 669–681 (1986).
3. J.-C. Chen and C. Hu, Measurement of the float–zone interface shape for lithium niobate, *J. Crystal Growth* **149,** 87–95 (1995).
4. J.-C. Chen and C. Hu, Measurement of the surface temperature in the float zone of $LiNbO_3$, *J. Crystal Growth* **158,** 289–295 (1996).
5. C. Hu and J.-C. Chen, Experimental observation of interface shapes in the float zone of lithium niobate during a CO_2 laser melting, *Int. J. Heat Mass Transfer* **39,** 3347–3355 (1996).
6. C. W. Lan and S. Kou, Thermocapillary flow and melt/solid interfaces in floating-zone crystal growth under microgravity, *J. Crystal Growth* **102,** 1043–1058 (1990).
7. C. W. Lan and S. Kou, Heat transfer, fluid flow and interface shapes in floating-zone crystal growth, *J. Crystal Growth* **108,** 351–366 (1991).
8. C. W. Lan and S. Kou, Effects of rotation on heat transfer, fluid flow and interfaces in normal gravity floating-zone crystal growth, *J. Crystal Growth* **114,** 517–535 (1991).
9. J. C. Chen, C. F. Chu and W. F. Ueng, thermocapillary convection and melt–solid interface in the floating zone, *Int. J. Heat Mass Transfer* **37,** 1733–1748 (1994).
10. J. C. Chen and C. F. Chu, Numerical computation of fluid flow of floating-zone crystal growth of Molybdenum, *Int. J. Heat Mass Transfer* **38,** 1841–1853 (1995).
11. J. C. Chen and G. H. Chin, Linear stability analysis of thermocapillary convection in the floating zone, *J. Crystal Growth* **154,** 98–107 (1995).
12. K. Shigematsu, Y. Anzai, S. Morita, M. Yamada and H. Yokoyama, Growth conditions of subgrain-free $LiNbO_3$ single crystals by the Czochralski method, *Jpn. J. Appl. Phys.* **26,** 1988–1996 (1987).
13. Y. Anzai, S. Kimura, T. Sawada, T. Rudolph and K. Shigematsu, Measurement of density, viscosity and surface tension of molten lithium niobate, *J. Crystal Growth* **134,** 227–234 (1993).
14. J. C. Brice, The cracking of Czochralski-grown crystals, *J. Crystal Growth* **42,** 427–430 (1977).